Enhanced superplasticity in an Al-alloyed multicomponent Mn–Si–Cr–C steel

H. Zhang [*], K.G. Pradeep, S. Mandal, D. Ponge, P. Choi, C.C. Tasan, D. Raabe [*]

Max-Planck Institut für Eisenforschung, Max-Planck Str. 1, 40237 Düsseldorf, Germany

Abstract

Excellent superplasticity (elongation ∼720%) is observed in a novel multi-component (Mn–S–Cr–Al alloyed) ultrahigh carbon steel during tensile testing at a strain rate of $2 \times 10^{-3} \, s^{-1}$ and a temperature of 1053 K (just above the equilibrium austenite–pearlite transformation temperature). In order to understand superplasticity in this material and its strong Al dependence, the deformation-induced microstructure evolution is characterized at various length scales down to atomic resolution, using X-ray diffraction, scanning electron microscopy, electron backscatter diffraction, energy-dispersive X-ray spectroscopy and atom probe tomography. The results reveal that 1 wt.% Al addition influences various microprocesses during deformation, e.g. it impedes Ostwald ripening of carbides, carbide dissolution, austenite nucleation and growth and void growth. As a result, the size of the austenite grains and voids remains relatively fine (<10 μm) during superplastic deformation, and fine-grained superplasticity is enabled without premature failure.
© 2013 Acta Materialia Inc. Published by Elsevier Ltd. All rights reserved.

Keywords: Steel; Superplasticity; Aluminum; Grain growth; Void

1. Introduction

Superplasticity relates to a promising forming procedure that can be used to render steel components in nearly arbitrary shape without machining. Various studies on grain refinement by thermomechanical processing have been reported during the past few decades [1–13], revealing promising pathways for realizing superplastic characteristics in steels. However, the effects of alloying elements on superplasticity have been rarely studied in detail despite their important role in controlling those microstructures that enable superplasticity [14–19]. Few examples in the literature focus on the influence of Cr (a carbide stabilizing element) [14] and Si (a ferrite stabilizing element) [15] on microstructures suited for superplasticity. It was revealed that Cr stabilized the carbides at ferrite grain boundaries

so that ferrite growth was suppressed during superplastic deformation. Si increases the equilibrium austenite–pearlite transformation temperature (Ae_1) and maintains a sufficient amount of carbides at relatively high temperature. We recently studied the influence of alloying on superplasticity [16] and observed that Mn–Si–Cr alloying alters the precipitation behavior of carbides and promotes the formation of a relatively fine (ferrite + carbide) microstructure, which is beneficial for superplastic deformation below Ae_1. The role of other alloying elements has so far not been investigated. For the case of Al, a frequently used deoxidizer in steel synthesis, the interest has been limited to high-strain-rate superplasticity of high Al (10 wt.%) powder-metallurgical alloys [19], while lower regimes of Al alloying (<2 wt.%), which would allow avoiding graphitization during casting (and also powder-metallurgy routes), were not studied. This is surprising, since two major influences of Al, namely, (i) increase of the equilibrium (Ae_1) temperature [15]; (ii) suppression of the precipitation of continuous network carbides and refinement of the inter-lamellar spacing of pearlite [17,18], may both have a

---

 * Corresponding authors.

E-mail addresses: h.zhang@mpie.de (H. Zhang), d.raabe@mpie.de (D. Raabe).

direct influence on the superplastic behavior of steels. The role of a third effect, viz., the precipitation of AlN [20], can be neglected when N is below 30 ppm, such as in this study. The first influence strongly affects the microstructure evolution during superplastic deformation around Ae_1, and therefore is expected to cause significant effects on the superplastic behavior. The second effect contributes to the suppression of network carbides at austenite grain boundaries during thermomechanical treatment (before superplastic forming). During superplastic deformation, this influence of Al could also affect the superplasticity of initially formed martensitic microstructures with saturated carbon by changing the formation process of the (ferrite + carbide) microstructure below Ae_1 (e.g. carbide precipitation, dynamic recrystallization of ferrite), similar to the effect of Si as discussed earlier [16]. One should note that the influence of Al on the precipitation of carbides during superplastic deformation can be avoided in microstructures where carbides are already present in the initial state.

These aspects encourage us to exploit the potential of Al alloying for improving the superplasticity of steels and elucidate the mechanisms involved. Therefore, in this work, a novel steel is designed originating from the previously introduced Mn–Si–Cr alloyed system [16], focusing specifically on the role of Al alloying. The microstructural states during superplastic deformation are characterized down to atomic resolution to reveal the microstructure in detail and detect possible Al segregation along the ferrite/austenite and austenite interfaces [21].

2. Experimental methods

2.1. Alloy design strategy

The compositions of two steels are listed in Table 1. The starting point of the alloys is the previously introduced Mn–Si–Cr alloying system [16]. Manganese is added to improve hardenability and to ensure microstructure homogeneity in warm-rolled plates after thermomechanical processing. Si alloying prevents the formation of a coarse carbide network during thermomechanical processing whereas Cr stabilizes spherical carbides and suppresses graphitization. Ultrahigh carbon content is used to ensure the formation of a sufficient amount of spherical carbides during superplastic deformation. In addition to these alloying elements, a medium amount (~1 wt.%) of Al is added

to one of the steels to investigate the influence of Al on superplasticity.

2.2. Processing of the alloys

The steels were produced by vacuum induction melting and cast in 70 mm × 70 mm billets. For homogenizing, as-cast 70 mm thick plates were hot-rolled to 35 mm at 1323 K, and subsequently air-cooled to room temperature. The hot-rolled plates were then annealed at 1173 K for 60 min, followed by water quenching to room temperature, so that refined (martensite + spherical carbide) microstructures were obtained. The plates were further heated to 923 K, warm-rolled down to 20 mm and water quenched to room temperature. After the warm-rolling process, ferrite plus spherical carbide microstructures were obtained, which are used as the initial microstructures prior to superplastic deformation.

The Ae_1 and A_{cm} temperatures were calculated by ThermoCalc using the TCFE5 database [22,23] and then experimentally verified via dilatometer tests using a Bähr Dil805 A/D quenching and deformation dilatometer (see Table 2).

2.3. High temperature tensile testing

Bone-shaped flat tensile specimens (gauge length 10 mm) machined from the plates with ferrite plus spherical carbide microstructures were used for high temperature tensile testing on a Zwick/Roell ZMART.PRO tensile machine. These specimens were heated through thermal convection. Temperature control of the specimens was carried out by a thermocouple connected with both the furnace and the specimen. Stress and strain were measured by a force-sensing socket and displacement sensor. Argon atmosphere was used to minimize surface oxidation.

The tensile tests were conducted at a strain rate of $2 \times 10^{-3} \, s^{-1}$ and different temperatures around Ae_1 in the range between 873 and 1123 K. For each deformation condition, three to five tensile specimens were used. Interrupted tensile tests were performed by taking specimens at different strains.

During the tests, to achieve a homogeneous temperature distribution, the tensile specimens were held for 2 min at deformation temperature prior to mechanical loading. The tensile axis was parallel to the hot- and warm-rolling direction. After tensile testing, an air pistol was

Table 1
Chemical compositions of the steels used in this investigation.

Alloying elements		C	Mn	Si	Cr	Al	N	Fe
Al-free	wt.%	1.32	2.26	1.73	1.09	–	0.0024	Bal.
	at.%	5.77	2.16	3.24	1.10	–	0.009	Bal.
Al-alloyed	wt.%	1.29	2.31	1.80	1.05	0.99	0.0026	Bal.
	at.%	5.59	2.18	3.34	1.05	1.91	0.010	Bal.

Table 2
The Ae_1 and A_{cm} temperatures of the steels used in this investigation. A_{cm}: equilibrium austenite-cementite transformation temperature.

	Ae_1 (K)	A_{cm} (K)
Al-free	1003	1283
Al-alloyed	1033	1233

immediately used to blow air onto the specimens, in order to realize fast cooling.

2.4. Scanning electron microscopy (SEM) and electron backscattered diffraction (EBSD)

SEM specimens were prepared by standard mechanical grinding and polishing procedures. Secondary electron imaging and the EBSD technique (step size 100 nm) were used to determine void distribution and phase fractions, both performed on a JEOL-6500F high-resolution field-emission scanning electron microscope operated at 15 kV [24]. The data collected by EBSD were analyzed using the TSL OIM analysis software. The image quality (IQ) of the EBSD maps serves as a qualitative measure for the defect content of the crystals [25,26]. Perfect crystal regions have a high IQ value (light) while regions with a high defect density (e.g. interfaces, high-dislocation densities) have a low IQ value (dark) [27]. Therefore, the IQ measure (also combined with microstructure morphology) was here used to distinguish ferrite and martensite [28,29]. In addition, energy-dispersive spectroscopy (EDS) line scanning was also conducted on JEOL-6500F to reveal the distribution of alloying elements across interfaces.

2.5. X-ray diffraction (XRD)

The volume fraction of spherical carbides present in the initial ferrite plus spherical carbide microstructures was measured by using XRD, in order to compare these results with those obtained from the EBSD measurements. Specimens for XRD measurements were mounted on a Huber-2 goniometer and were exposed to Co Kα radiation ($\lambda = 1.79$ Å). The Metero0D detector swept the 2θ range from 40° to 120° with the step size $\Delta 2\theta = 0.05°$ for a count time of 20 s per step. Rietveld analysis using MAUD software (Version 2.33) was conducted to estimate the volume fraction of spherical carbides as well as the lattice parameters of ferrite.

2.6. Atom probe tomography (APT)

The distribution of alloying elements at original austenite grain boundaries as well as the inside of austenite grains after superplastic deformation were analyzed by APT [30–32]. Needle-shaped APT specimens were prepared using a dual-beam focused ion beam (FIB, FEI Helios Nanolab 600i) device following the procedures described in Ref. [33]. APT analysis was performed with a local electrode atom probe (LEAP™ 3000X HR, Cameca Instruments)

in voltage mode at ∼60 K. The pulse fraction and repetition rates were 15% and 200 kHz, respectively. Data reconstruction and analysis were carried out using the IVAS 3.6 software by Cameca Instruments.

The experimentally observed frequency distribution of individual elements in the measured APT data set was compared with a theoretical derived binomial distribution, in order to evaluate the degree of randomness in the analyzed volume [34,35]. A normalization parameter, μ, was defined as

$$\mu = \sqrt{\frac{\chi^2}{N + \chi^2}}$$

where χ^2 is the quantified statistical parameter that measures the deviation of an experimentally determined distribution to the binomial distribution and N is the number of sampled blocks in the analysis. The randomness is measured by the parameter μ, independent of sample size, and returns a value between 0 and 1, where 0 stands for complete randomness and 1 indicates solute clustering or deviation from randomness [36].

3. Results

3.1. Initial microstructures prior to tensile testing

Phase distribution maps in Fig. 1a and c reveal that the initial microstructures of Al-free and Al-alloyed steels both consist of ferrite (green color) and spherical carbides (blue color). The dispersed carbides reveal bimodal size distribution. Here the submicron and nanometer scales are classified to be 0.5–1.5 μm and <0.5 μm, which are denoted by black and red arrows, respectively. The estimated volume fractions of carbides from Fig. 1a and c are 10.9% and 9.7%, respectively. Fig. 1b and d shows the corresponding inverse pole figure maps of ferrite, where high angle grain boundaries are indicated by >15°. Most of the ferrite grains are recrystallized. The size of the ferrite grains are mostly within the range of 1–2 μm. Some large grains with a size of 5–6 μm also exist, but only as a small volume fraction. The average diameters of ferrite grains for Al-free and Al-alloyed steels are 1.03 and 0.98 μm (statistic range: 0.5–6 μm), respectively.

Compared to the EBSD results, the XRD results reveal a slightly higher volume fraction of carbides, namely, 14.2% for Al-free and 12.5% for Al-alloyed steel. It is also verified from the XRD analysis that the lattice parameter of ferrite is similar to that of the two steels (2.869 Å for the Al-free steel and 2.873 Å for the Al-alloyed steel). In total, the morphology, phase fraction and matrix lattice parameter of these two (ferrite + spherical carbide) microstructures are similar. The main difference lies in the overall alloy composition and the distribution of alloying elements in the microstructures, i.e. the ferrite in the Al-alloyed steel contains Al in solid solution. An EDS line scan across a submicron-sized carbide in the Al-alloyed steel is shown
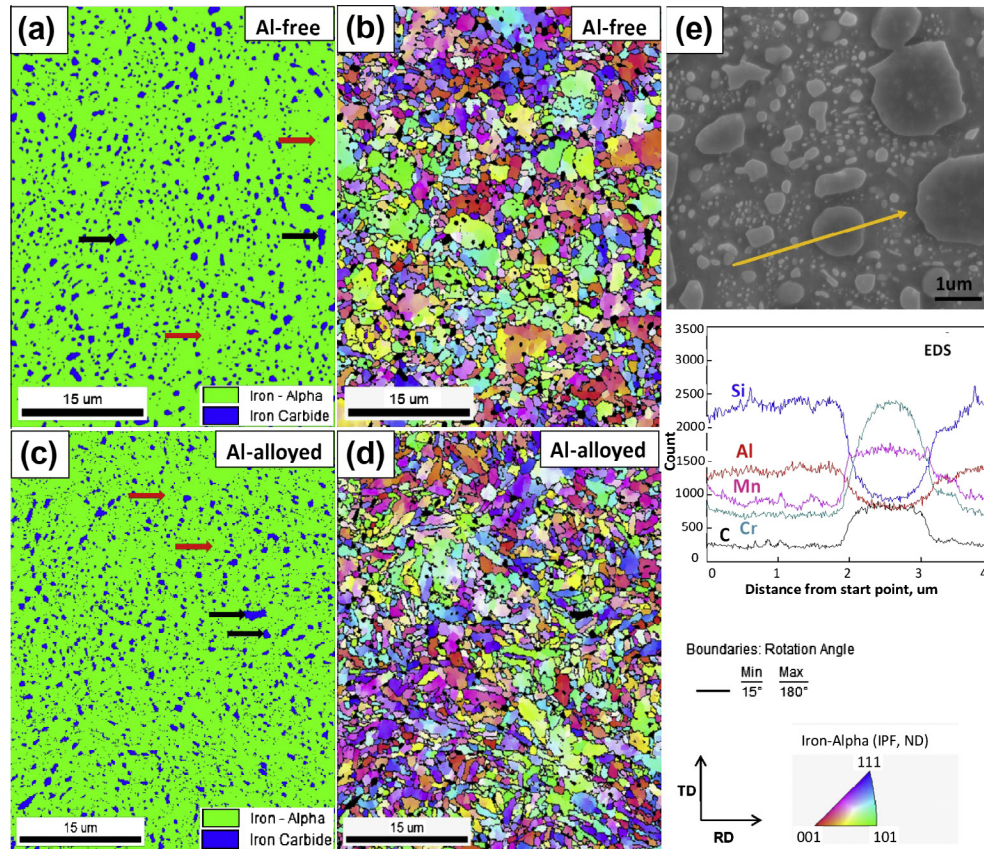
Fig. 1. Phase distribution maps of the initial microstructures in (a) Al-free and (c) Al-alloyed steels; corresponding inverse pole figure (IPF) maps of ferrite in (b) Al-free and (d) Al-alloyed steels; (e) EDS line scanning results across a submicron carbide in the Al-alloyed steel (yellow line). Submicron (0.5–1.5 μm) and nanometer (<0.5 μm) carbides denoted by black and red arrows, respectively. (For interpretation of the references to color in this figure legend, the reader is referred to the web version of this article.)

in Fig. 1e. On this carbide, Mn and Cr are enriched while Si and Al are depleted.

3.2. Tensile elongation

The tensile elongation to failure values at a strain rate of 2×10^{-3} s^{-1} and different temperatures around Ae_1 are
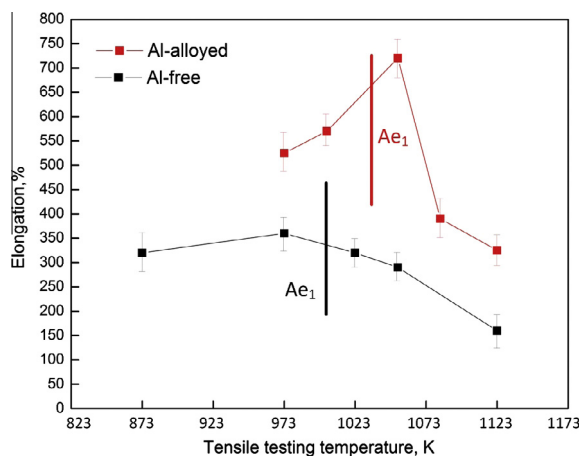

Fig. 2. Tensile elongation values at different temperatures around Ae_1 (strain rate: 2×10^{-3} s^{-1}).

shown in Fig. 2. It can be seen that the Al-alloyed steel exhibits much higher elongations compared to the Al-free steel, especially just above the Ae_1 temperature (1053 K). A distinct peak elongation value (∼720%) of the Al-alloyed steel occurs at 1053 K. In contrast, an obvious peak elongation value is not found for Al-free steel. For both steels, the elongation values drop drastically with increasing temperature above Ae_1.

3.3. Microstructures near the tensile test fracture zones

Fig. 3a–c shows joint phase plus IQ EBSD maps of the Al-free steel taken near the fracture zone after the tensile tests at 973, 1053 and 1123 K, respectively. The phases existing in the near fracture zone after the tensile tests (followed by water quenching) reveal the deformed microstructures occurring at the high temperatures. The presence of martensite (dark green color) and retained austenite (red color) in Fig. 3a, for example, reveals that austenite is formed during the tensile tests and partially transforms to martensite during cooling. At 973 K (30 K below Ae_1), apart from austenite and carbides, some ferrite (denoted by black arrows in Fig. 3a), which is characterized by its high image quality (light green color) and equiaxed shape,
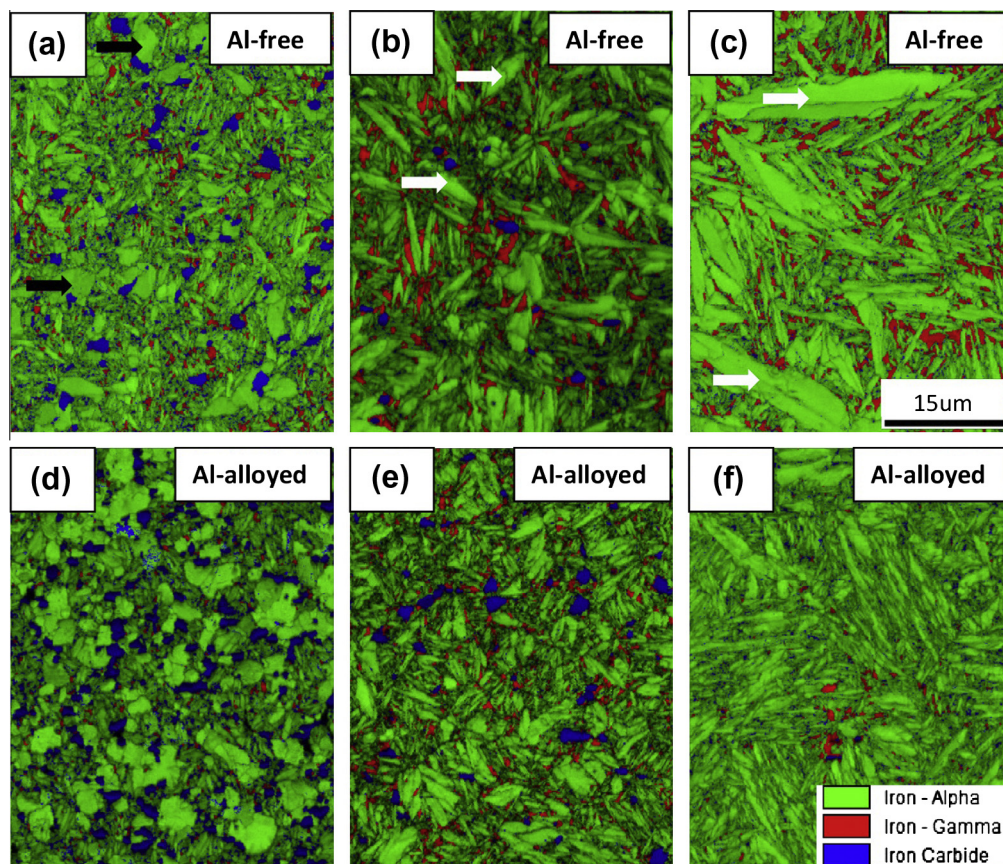
Fig. 3. Joint phase plus IQ EBSD maps of Al-free steel near fracture zone after tensile tests at (a) 973 K, (b) 1053 K and (c) 1123 K; joint phase plus IQ EBSD maps of Al-alloyed steel near fracture zone after tensile tests at (d) 973 K, (e) 1053 K and (f) 1123 K. Ferrite (with high IQ and equiaxed shape) and martensite (with high IQ and plate shape) denoted by black arrows and white arrows, respectively. Strain rate: $2 \times 10^{-3}\ \mathrm{s}^{-1}$. (For interpretation of the references to colour in this figure legend, the reader is referred to the web version of this article.)

prevails in the deformed microstructure. At 1053 K (50 K above Ae_1), the ferrite transforms entirely into austenite. Consequently, the deformed microstructure at 1053 K consists of austenite and carbides. At 1123 K, the carbides dissolve fast and only austenite exists in the deformed microstructure. From the joint phase plus IQ EBSD maps in Fig. 3d–f, it can be confirmed that the same transformation process as that of Al-free steel occurs during tensile testing of the Al-alloyed steel at 973, 1053 and 1123 K. It should be noted that not all α-Fe phases with high image quality in these cases are ferrite. Some plate-shaped zones (light green color) can be distinguished as martensite, as denoted by white arrows in Fig. 3b and c.

Fig. 4 shows the corresponding inverse pole figure maps of retained austenite in Fig. 3. It can be seen that the austenite grains formed in the Al-alloyed steel during the tensile tests are obviously finer than those in the Al-free steel at each deformation temperature.

3.4. Microstructures observed after interrupted tensile tests

The microstructures of the Al-free and Al-alloyed steels after interrupted tensile testing (1053 K) at different engineering strains are shown in Fig. 5a and b. As in Fig. 3,

it should be considered that the martensite (dark green color and/or with plate shape) is transformed from the austenite present at 1053 K during cooling after the tensile testing, while some of the austenite (red color) is retained. At a strain of 48%, the austenite transformation from the initial microstructure is almost complete in the Al-free steel while austenite transformation has just started in the Al-containing variant. Fig. 5a reveals ∼80 vol.% martensite and Fig. 5b shows ∼90 vol.% ferrite. Martensite and ferrite can be differentiated from each other through the IQ and morphology. In addition, the carbide volume fraction and size in the Al-free alloy are obviously larger, in comparison with Al-alloyed material. At 120% strain, austenite transformation is also completed in the Al-alloyed steel. Fig. 6 shows the volume fraction of carbides at the different strain levels (at 1053 K and a strain rate of $2 \times 10^{-3}\ \mathrm{s}^{-1}$) estimated using EBSD analysis. With the increase in strain (from 48% to 240%), the volume fraction of carbides in the Al-free steel decreases significantly from 20% to 5%. However, the decrease in the carbide content in the Al-alloyed steel during deformation proceeds relatively slowly. Within the wide strain range of 240–720%, the volume fraction of carbides essentially remains constant. For both steels there exists a strain range shortly after the onset of deformation
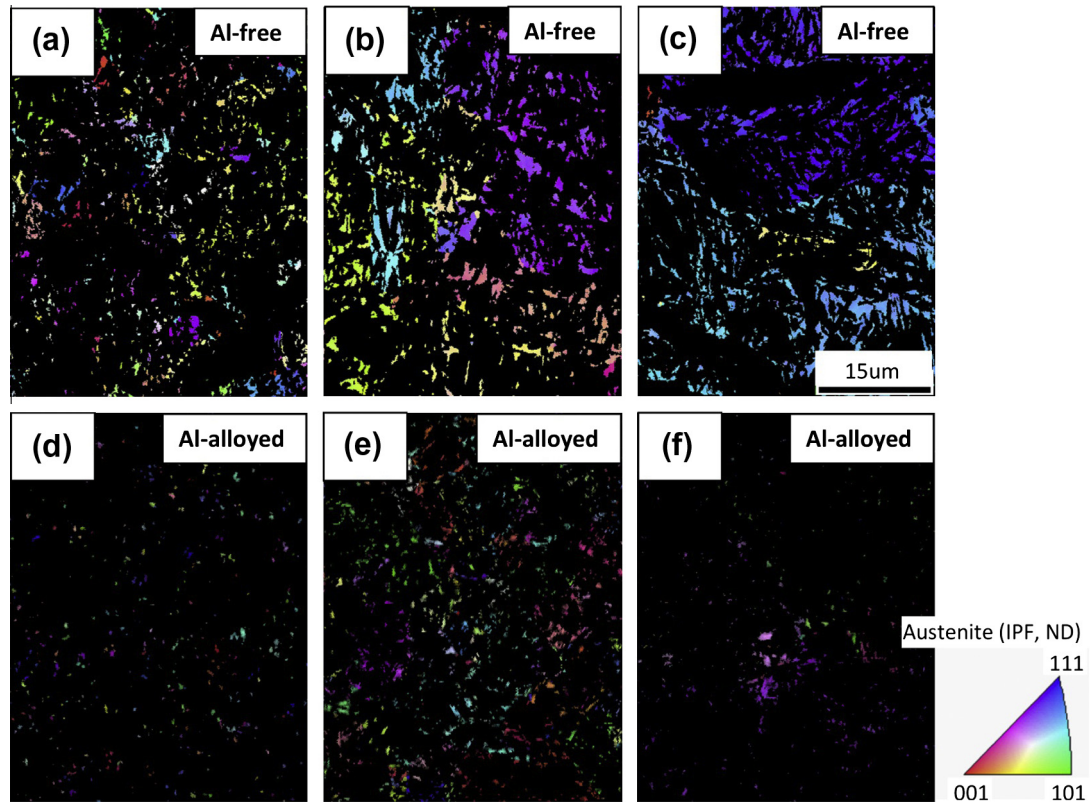
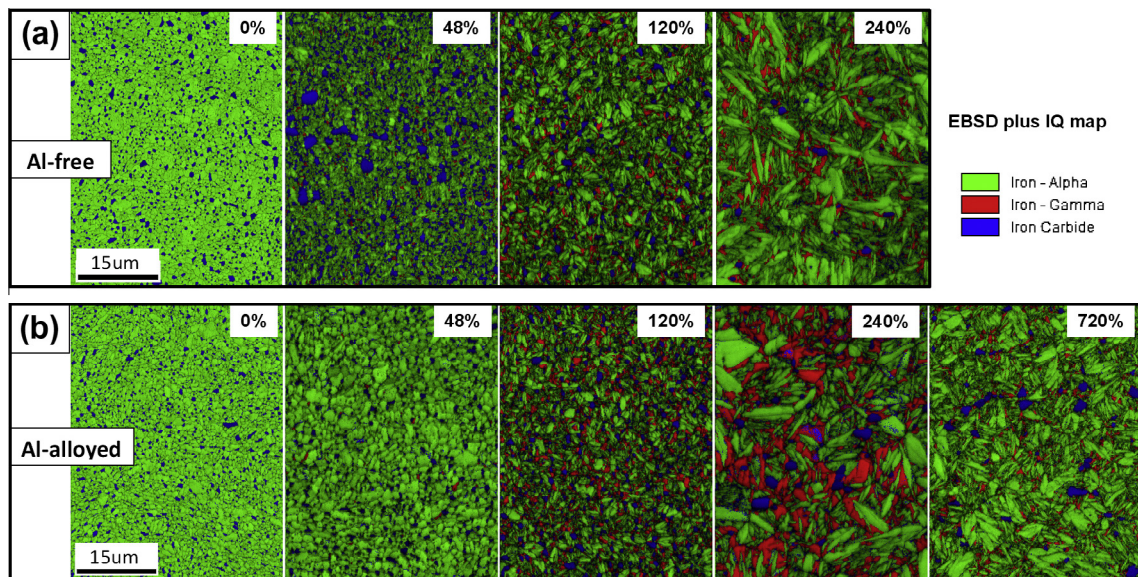Fig. 4. Corresponding inverse pole figure (IPF) maps of retained austenite in Fig. 3.

Fig. 5. Joint phase plus IQ EBSD maps after interrupted tensile tests (1053 K, strain rate: $2 \times 10^{-3}\,\mathrm{s}^{-1}$) at different engineering strains for (a) Al-free steel and (b) Al-alloyed steel (0%: initial microstructures prior to tensile testing).

where the volume fraction of carbides increases with increasing strain (0–48% for the Al-free steel and 48–120% for the Al-alloyed material). In addition, the size of carbides in both steels increases during deformation, which is revealed by comparing the initial microstructures with those deformed up to specific strain levels (e.g. 240% strain for the Al-alloyed steel).

3.5. Element distribution at interfaces and grain boundaries

Fig. 7a shows the near-fracture-zone microstructure of the Al-alloyed steel after tensile testing at 973 K (below Ae_1) and an initial strain rate of $2 \times 10^{-3}\,\mathrm{s}^{-1}$ (see also Fig. 3d). The microstructure is composed of ferrite (light green color), martensite (dark green color, transformed
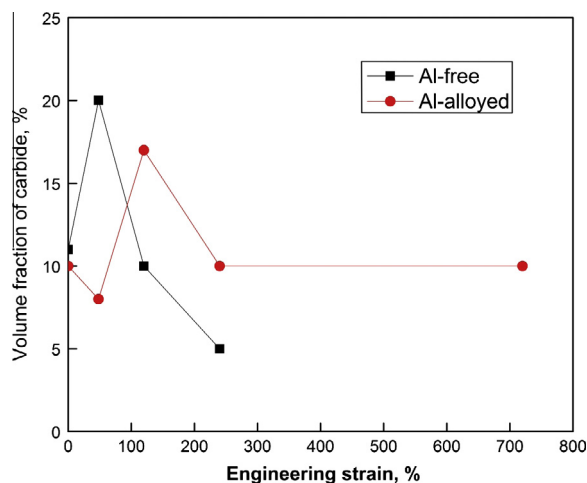
Fig. 6. Volume fraction of carbides at different strain levels (1053 K, strain rate: $2 \times 10^{-3}\,s^{-1}$) estimated by EBSD analysis.

shown in inset of Fig. 8a and b, which contains a much higher carbon concentration ($\sim$16 at.%) than the martensite. The error bars represent the 2σ standard deviation. It is also observed that the other alloying elements such as Mn, Si, Cr and Al are distributed homogeneously in both phases, in the retained austenite and also in the martensitic matrix. Fig. 8c and d shows the binomial frequency distribution analysis for estimating the Al homogeneity near the original austenite grain boundary and inside the austenite grain, respectively. The parameter μ, used to evaluate the degree of randomness between the two different measurements, returns a value close to 0.06 in both cases. This observation indicates that Al is randomly distributed. No Al segregation occurs near the original austenite grain boundary during tensile testing. Due to the absence of carbides in these APT specimens, the average measured Al concentration (2.8 at.%) is higher than the bulk concentration (1.9 at.%).

3.6. Void formation

Fig. 9a–c shows the void distribution observed in the Al-free steel near the fracture region after tensile tests at 973, 1053 and 1123 K, respectively. The insets in these figures clearly reveal that the void density (i.e. area fraction of voids measured by ImageJ software [38]) drops with the increase in deformation temperature. Similar results are also observed for the Al-alloyed steel after tensile tests at 973, 1053 and 1123 K, as shown in Fig. 9d–f. In comparison with the Al-free steel, the Al-alloyed material contains a higher density of voids. The void size observed in the Al-alloyed steel (Fig. 9f) is even larger than that found in the Al-free steel (Fig. 9c) after tensile testing at 1123 K. However, it is important to note that the void size ($<$10 μm) in the Al-alloyed steel (Fig. 9d and e) is similar

from austenite) and carbides (blue color). An EDS line scan was conducted across the martensite/ferrite interface according to the scan direction indicated by the arrow. The distribution of Al and Si (as shown in Fig. 7b and c) reveals that Al and Si are segregated at the ferrite/martensite interface. In contrast, Cr and Mn are depleted, as shown in Fig. 7d and e. The segregation of Al at ferrite/martensite interface is consistent with previous results [21].

Fig. 8a and b shows the one-dimensional (1-D) concentration–depth profile, measured by APT, of retained austenite and the matrix (consisting of martensite, Fig. 3e) near the original austenite grain boundary after a tensile test conducted at 1053 K (above Ae_1) and an initial strain rate of $2 \times 10^{-3}\,s^{-1}$ in the Al-alloyed steel [37]. The retained austenite is revealed as a carbon-enriched zone measured locally using a cylinder of 1.5 nm radius, as
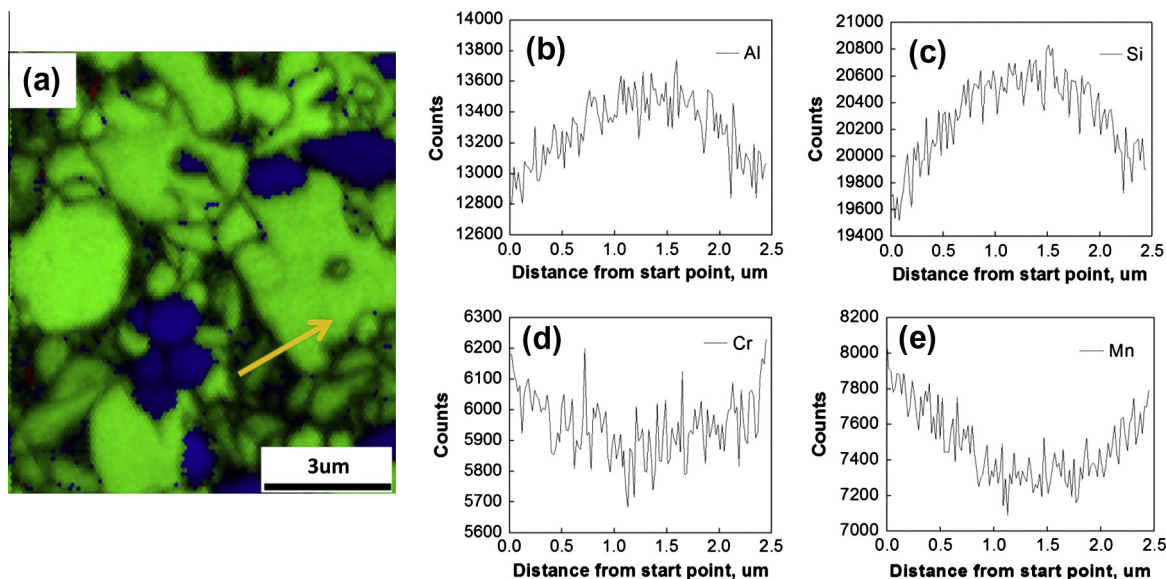

Fig. 7. (a) An enlarged phase plus IQ EBSD map of Al-alloyed steel near fracture zone after tensile testing at 973 K and a strain rate of $2 \times 10^{-3}\,s^{-1}$ (see also Fig. 3d). EDS line scanning results of (b) Al (c) Si (d) Cr and (e) Mn in the arrow direction (across martensite/ferrite interface).
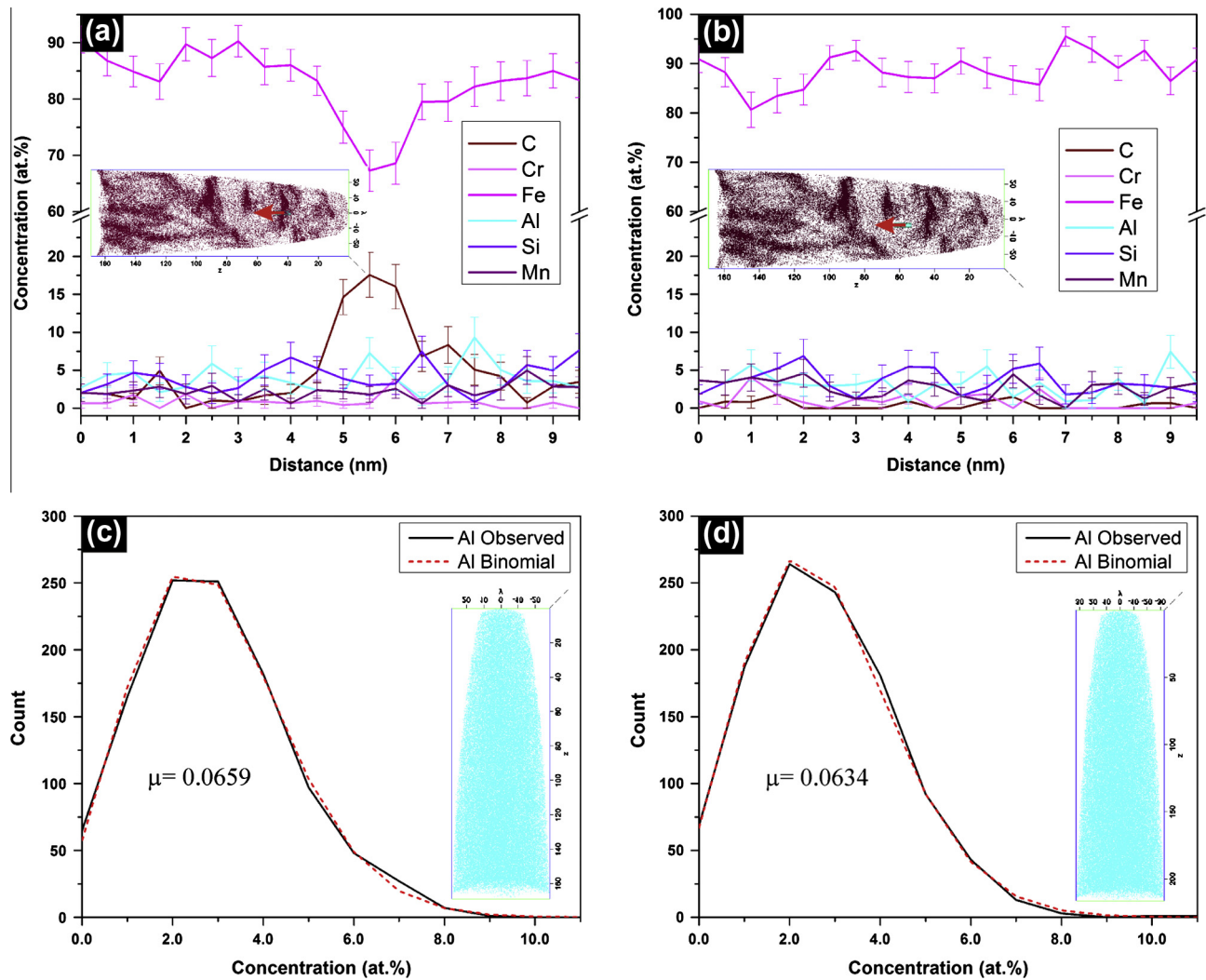
Fig. 8. 1-D concentration profile for (a) retained austenite and (b) martensitic matrix near original austenite grain boundary after tensile testing at 1053 K and 2×10^{-3} s^{-1} (Al-alloyed steel) measured using a cylinder of 1.5 nm radius and 0.5 nm bin width. Inset showing the elemental map of C in an analyzed volume of $58 \times 58 \times 168$ nm^3 with the arrow in red indicating the localized measurement direction along the cylinder; Distribution analysis for Al homogeneity (c) near original austenite grain boundary and (d) the inside of original austenite grain after tensile testing at 1053 K and 2×10^{-3} s^{-1} (Al-alloyed steel) measured with a minimum of 100 ions per bin. (For interpretation of the references to color in this figure legend, the reader is referred to the web version of this article.)

to that in the Al-free steel (Fig. 9a and b) after tensile testing at 973 and 1053 K, respectively, although the deformation period to which the Al-alloyed steel was subjected was much longer at 973 and 1053 K (larger elongation as shown in Fig. 2).

4. Discussion

4.1. Microstructure evolution during tensile testing

Fig. 5 reveals that austenite transformation occurs during tensile testing at high temperatures (e.g. 1053 K). The size and volume fraction of carbides also change with increasing strain. The applied strain can lead to the accumulation of lattice defects (e.g. dislocations) which promote pipe diffusion of carbon [39].

At low strain levels, the defect density is expected to be too low to profoundly support carbide dissolution through pipe diffusion. Consequently, the volume fraction of carbides even seems to increase (rather than decrease) during the early stage of tensile testing, i.e. prior to the strain of 48% for the Al-free steel and 120% strain for the Al-alloyed steel, as indicated in Fig. 6. Compared to the initial microstructures observed before tensile testing, the microstructures found after the interrupted tensile tests at 48% strain (Al-free steel, Fig. 5a) and at 120% strain (Al-alloyed steel, Fig. 5b) contain more carbides. At first sight this observation seems to be questionable, since austenite transformation during the early stages of the tensile tests would be expected to consume carbon from carbides. Therefore, the source of further carbon supply from the initial microstructures needed for the increase of the carbide volume
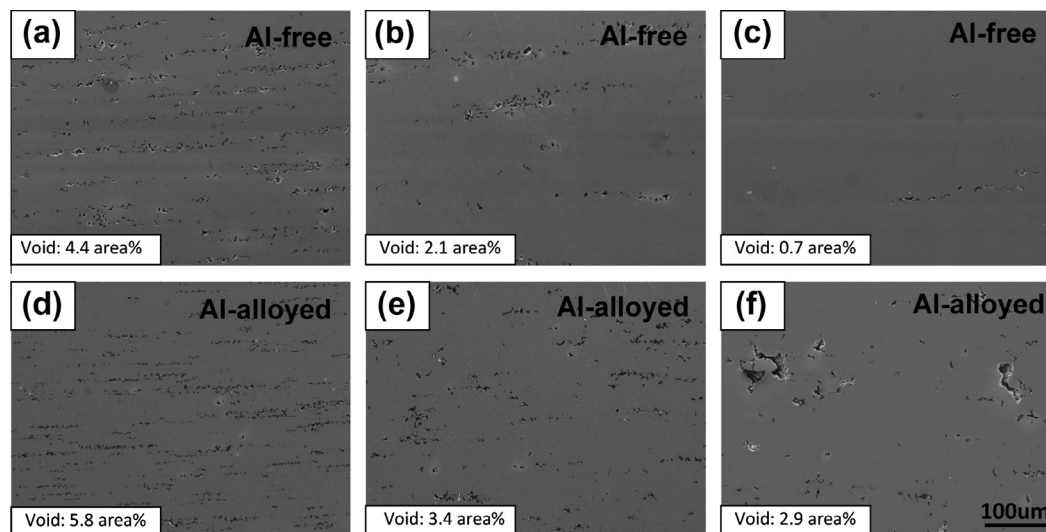
Fig. 9. Void distribution near fracture zones after tensile tests at a strain rate of 2×10^{-3} s^{-1}. Al-free steel: (a) 973 K, (b) 1053 K and (c) 1123 K; Al-alloyed steel: (d) 973 K, (e) 1053 K and (f) 1123 K.

fraction and the formation of austenite during the early stage of tensile testing is discussed in the following. As mentioned above, the estimated volume fraction of carbides is larger according to the XRD measurements when compared to the corresponding EBSD measurements conducted on the same specimens. This observation suggests that the ultrafine carbides present in the initial microstructures (especially those with a size of several nanometers) can hardly be detected due to the limited resolution of EBSD. The volume characterization conducted by using XRD has hence a higher probability to map ultrafine carbides leading altogether to a higher volume fraction estimation from the XRD data. We therefore assume that the XRD data provide a more realistic estimate of the true carbide amount. In fact, the volume fraction of carbides measured by XRD could even still be lower than the actual value (the equilibrium amount of carbides in the initial microstructures calculated as ~20 vol.% by ThermoCalc) because of the small grain size effect on the broadening of the XRD peaks. However, an increase in the volume fraction of carbides being measured by EBSD indicates that the coarsening of the carbides follows classical Ostwald ripening [16], resulting in a higher amount of larger carbides (e.g. with a size of >200 nm), which can be more easily detected by EBSD. The coarsened carbide size distributions observed in the microstructures that were mapped after the interrupted tensile tests at 48% strain (Al-free steel, Fig. 5a) and at 120% strain (Al-alloyed steel, Fig. 5b) relative to the size distributions observed in the initial microstructures also suggest the occurrence of conventional Ostwald ripening. It should be noted that the oversaturation of alloying elements in the ferrite matrix for the case of the initial microstructures can be neglected since the lattice parameter of ferrite does not change much compared to that of pure α-Fe (see Section 3.1).

At large strain levels when a high density of defects is induced, the dissolution of carbides through pipe diffusion

becomes relevant [40]. Therefore, there exists a stage during which the volume fraction of carbides decreases with increasing strain for both types of steels (i.e. in the strain range between 48% and 240% for the Al-free steel and between 120% and 240% for the Al-alloyed steel in Fig. 6). This stage is hereafter referred to as the "later stage" of the tensile tests in order to differentiate it from the "early stage" shortly after the onset of the tensile tests. It is reasonable to assume that the defects induced by the superplastic deformation are more preferably located near the austenite/large-sized carbide interfaces due to the deformation incompatibility between austenite and large carbides (with a size of >0.5 μm). Therefore, the dissolution of these carbides occurs primarily during the later stage, leading to a decrease in the carbide volume fraction. Consequently, a small number of micron-sized carbides (1–3 μm, size increase due to Ostwald ripening) exists after the interrupted tensile tests at a strain of 240%.

In order to reveal the microstructure evolution during tensile testing (e.g. at 1053 K), a schematic diagram is shown in Fig. 10. During the early stage of the tensile test, Ostwald ripening determines the size and volume fraction of the carbides. The submicron-sized carbides coarsen at the expense of the nanometer-sized carbides and the number of submicron-sized carbides increases. Due to the low dislocation density at this stage, complete dissolution of carbides with a size of >0.5 μm does not occur. Therefore, the total volume fraction of carbides remains almost stable during the early tensile stage. With increasing strain, the dislocation density increases, resulting in the dissolution of relatively large carbides (>0.5 μm). Carbide coarsening is due to Ostwald ripening. Consequently, some micron-sized carbides (1–3 μm) can remain in the microstructures although the carbide dissolution is considered the major process of carbide evolution during the later stages of the superplastic tensile test. In addition to these phenomena, austenite nucleation and growth occur simultaneously.
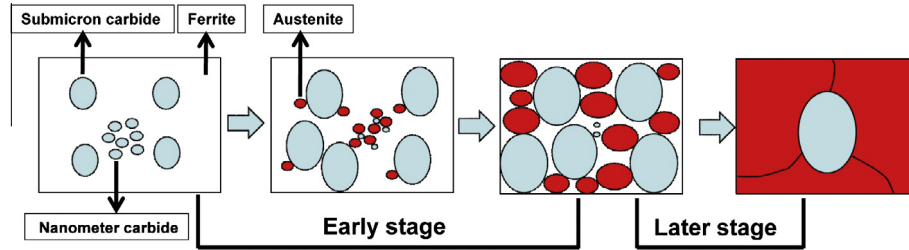
Fig. 10. Schematic diagram of the microstructure evolution during tensile testing at 1053 K (above Ae_1) and a strain rate of 2×10^{-3} s^{-1}.

During the early stages, austenite nucleates at the ferrite/carbide interfaces [41] and grows at a relatively slow rate due to carbide pinning. During the later stages, the volume fraction of carbides decreases due to dissolution and the pinning effect becomes weaker so that the growth rate of the austenite accelerates.

4.2. Necessary factors for austenite transformation during tensile testing

In the present work, austenite transformation occurs during tensile testing, even at temperatures below Ae_1 (e.g. 973 K, Fig. 3a and d). The peak elongation of the Al-alloyed material is observed at a temperature of 1053 K (20 K above Ae_1) when the ferrite present in the initial microstructure has fully transformed to austenite during the tensile tests. Therefore, we aim to understand the conditions required for austenite transformation and further explain the effect of the Al addition in that context on the here-observed enhanced superplasticity. The Gibbs free energy per mole (G_m) of ferrite and austenite at 1053 K was calculated using ThermoCalc and the G_m vs. carbon wt.% diagram is shown in Fig. 11. A minimum local carbon concentration (above which $\Delta G_{F \to A} < 0$, as denoted by the red dotted line) should be reached in order to achieve the necessary chemical driving force for austenite transformation from the ferrite. The increase in total interfacial energy as well as the strain energy accompanying the austenite transformation requires an even larger chemical driving force. This supports the assumption that local carbon enrichment is required for austenite nucleation during the tensile testing. In this context the occurrence of Ostwald ripening could provide the necessary local carbon enrichment at the ferrite/carbide interfaces where a carbon concentration gradient most probably occurs during the dissolution of small-sized carbides (e.g. nanometer scale <500 nm) and coarsening of large-sized carbides (e.g. submicron scale 0.5–1.5 μm). Regarding the changes in the total interfacial energy, the ferrite/carbide interfaces are also considered as favorable austenite nucleation sites due to their relatively high energy compared to low-angle grain boundaries [42].

From these observations we conclude that the deformation process promotes Ostwald ripening due to accelerated carbon diffusion via pipe diffusion. Therefore, deformation is considered to promote austenite transformation, even at temperatures below Ae_1 (e.g. 973 K). Fig. 3a and d clearly indicates that austenite transformation occurs during tensile testing at 973 K for both the Al-free and Al-alloyed variants. In contrast, austenite transformation does not occur during the isothermal holding of the Al-free steel at 973 K for 0.5 h (an identical time period as that used during tensile testing). This observation underlines that the tensile deformation can promote austenite transformation at high temperatures.

4.3. Effect of Al on controlling the microstructure evolution and void formation

4.3.1. Increase of equilibrium pearlite–austenite transformation temperature (Ae_1)

ThermoCalc predicts that 0.99 wt.% Al addition increases Ae_1 by 30 K (from 1003 to 1033 K). The increase in Ae_1 opposes austenite nucleation. Fig. 11 also shows that the minimum local carbon concentration required for austenite nucleation at 1053 K (neglecting the increase in the nucleation barrier due to interfacial energy) in Al-alloyed
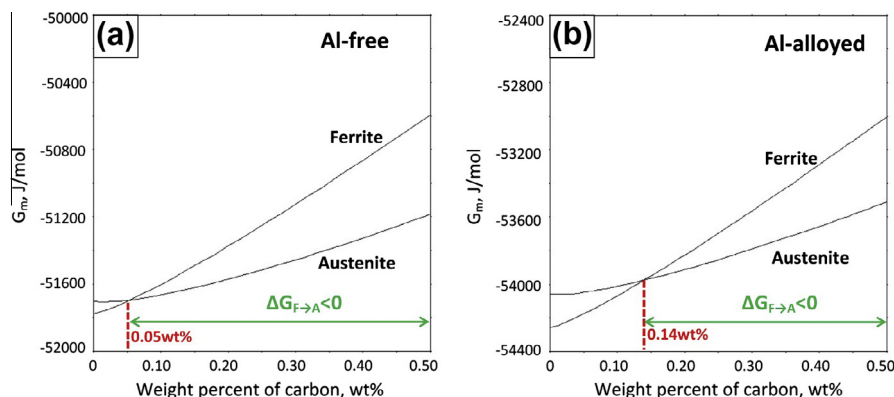

Fig. 11. The plot of Gibbs free energy per mole (G_m) of ferrite and austenite vs. weight per cent of carbon at 1053 K (calculated by Thermocalc).

steel (0.14 wt.%, Fig. 11b) is higher than that in Al-free steel (0.05 wt.%, Fig. 11a).

4.3.2. Retardation of Ostwald ripening and carbide dissolution

Fig. 1e suggests that there exists a concentration gradient of Al at the ferrite/carbide interface in the initial microstructures. This gradient, which is characterized by a relatively high Al concentration on the ferrite side, could suppress local carbon enrichment near ferrite/carbide interfaces by slowing down the carbon diffusion into Al-enriched ferrite zone during the early stages of the tensile tests. As a result, the dissolution of the nanometer-sized carbides and the Ostwald coarsening of submicron-sized carbides (controlled by carbon diffusion) are slowed down by Al alloying. Consequently, the carbide Ostwald ripening in the Al-alloyed steel is assumed to proceed very slowly during tensile testing at 1053 K. At a strain of 48%, the submicron-sized carbides do not coarsen significantly (Fig. 5b) while the submicron-sized carbides in the Al-free steel coarsen obviously (Fig. 5a). This indicates that Ostwald ripening proceeds faster in the Al-free steel.

In the same context we assume that the concentration gradient of Al also suppresses the dissolution of submicron-sized carbides during the later stages of the tensile tests. Fig. 6 reveals that the volume fraction of carbides existing in the Al-alloyed steel (10 vol.%) exceeds that observed in the Al-free steel (5 vol.%) after interrupted tensile tests at 1053 K and a strain of 240%.

4.3.3. Retardation of austenite growth

Besides the effect against austenite nucleation, Al-alloying can also slow down austenite growth due to two effects: (1) Al segregation at ferrite/austenite interfaces (as shown in Fig. 7b) suppresses the migration of ferrite/austenite interfaces and retards austenite growth into ferrite during the early stages of tensile testing; (2) the retardation of carbide dissolution during the later stages of tensile testing maintains the pinning effect of carbides on austenite grain growth. As a result, the size of austenite grains in the near fracture-zone microstructure of the Al-alloyed steels (Fig. 4e) is much finer than that found in Al-free steels (Fig. 4b) after tensile testing at 1053 K.

The expected Al segregation near the original austenite grain boundaries during tensile testing has not been detected by APT (Fig. 8c and d) in this study. Therefore, Al segregation near austenite grain boundaries cannot be considered to have an effect on controlling the superplastic behavior during the later stages of tensile testing when austenite is fully transformed from ferrite.

4.3.4. Retardation of carbon diffusion

The APT results (Fig. 8a and b) show that retained austenite contains more carbon in comparison with martensite (transformed from austenite at high temperatures). This suggests that the distribution of carbon in austenite grains at high temperatures is inhomogeneous. Consequently,

carbon-rich zones of austenite, being thermodynamically more stable, are retained at room temperature. After interrupted tensile testing at a strain of 240% (1053 K), the Al-alloyed steel exhibits a higher amount of retained austenite ([1]red color, Fig. 5b) than that observed in the Al-free variant (red color, Fig. 5a). This indicates that the distribution of carbon in the austenite grains of Al-alloyed steel is more inhomogeneous in comparison with the Al-free alloy. We assume in this context that Al alloying can retard the diffusion of carbon in the course of carbide dissolution and austenite transformation.

4.3.5. Retardation of void growth

Owing to the deformation incompatibility between soft phase and hard particles [43], the interfaces between austenite and the relatively large carbides with a size of >0.5 μm can act as the favorable nucleation sites for voids. Therefore, the microstructure consisting of a higher volume fraction of carbides exhibits a higher density of voids. As shown in Fig. 9, tensile testing at relatively low temperatures (e.g. 973 K) leads to the formation of more voids than that at relatively high temperatures (e.g. 1053 K) due to a higher volume fraction of carbides existing at lower temperatures (blue color in Fig. 3). This could also be considered as a reason why the elongation values obtained at 1053 K are higher than those obtained at 973 K in the Al-alloyed steel (red curve in Fig. 2). Also, in comparison with Al-free steel, Al-alloyed steel contains a higher density of voids at each test temperature. This is attributed to the longer deformation period (e.g. 20 min for Al-free steel and 60 min for Al-alloyed steel at 1053 K) and higher volume fraction of carbides in the Al-alloyed steel. In spite of this, the void size of the Al-alloyed material (Fig. 9d and e) is similar to that of the Al-free alloy (Fig. 9a and b) after tensile testing at 973 and 1053 K. This indicates that the void growth is suppressed by Al alloying. It is likely that the fine austenite grains in the Al-alloyed steel reduce the stress required to maintain the process of grain boundary sliding accommodated by slip [44]. Consequently, the applied stress level remains low (not much higher than grain boundary adhesive strength) during tensile testing. As a result, the void growth proceeds slowly and does not lead to premature failure. On the other hand, although solute Al (~1 wt.%) does not change the lattice parameter of ferrite in the initial microstructures, solute Al in ferrite or austenite increases the strength of the soft matrix (ferrite or austenite) by solid solution strengthening [45] during tensile testing at high temperatures and minimizes the strength difference between soft matrix and hard particles (carbides), which contributes to the suppression of void nucleation and growth [44]. It should be noted here that during tensile testing at very high temperatures (e.g. 1123 K), the duration of deformation period plays a very important role

---

[1] For interpretation of color in Figs. 3, 5 and 7, the reader is referred to the web version of this article.

in determining the void growth due to fast diffusion. This can lead to the formation of larger voids in the Al-alloyed steel (Fig. 9f) compared to the Al-free steel (Fig. 9c) since the deformation period to which the Al-alloyed steel is exposed (26 min) exceeds that used for the Al-free steel (13 min) at 1123 K.

4.4. Extension of superplastic deformation period due to the sluggish microstructure evolution controlled by Al-alloying

In this study, Ostwald ripening of carbides, carbide dissolution, carbon diffusion, austenite nucleation and growth as well as void formation are all retarded by Al alloying (1 wt.%). As a result, the entire evolution process of the microstructure and void formation in the Al-alloyed steel is slowed down during tensile testing, even at a huge strain of 720% at 1053 K. Consequently, the grain size of the matrix material (ferrite and/or austenite) remains very fine (<10 µm) during loading, which favors structural superplasticity controlled by grain boundary sliding [44]. This indicates that the role of alloying elements on the superplasticity of steels is significant. Our results hence enable an improved alloying approach for the design of steels with enhanced superplastic properties. More specifically, the idea is based on tailoring compositions for sluggish superplastic microstructure evolution and void formation, which leads to the maintenance of fine-grained microstructures during superplastic forming. One should mention that the Al-free steel (containing 1.73 wt.% Si) does not exhibit enhanced superplasticity although Si might have similar effects like Al. One possible reason for this might be that the Si addition used in this study was not sufficiently high. In future, Si alloying as well as the combination effect of Si and Al on superplasticity need to be further investigated.

5. Conclusions

Two initial ferrite plus spherical carbide microstructures, one without Al alloying and the other with 1 wt.% Al alloying, were superplastically deformed at a strain rate of $2 \times 10^{-3} \text{ s}^{-1}$ and different temperatures around Ae_1. The microstructure evolution during superplastic forming is characterized by Ostwald ripening of carbides, carbide dissolution and nucleation and growth of austenite. Void nucleation and growth occur simultaneously. Al alloying retards Ostwald ripening of carbides and austenite nucleation during the early stages of tensile testing. During the later stages of tensile testing, the dissolution of large-sized carbides (>0.5 µm), supported by the accumulation of dislocations, is also retarded by Al alloying. This enables grain boundary pinning. Also, Al segregation at the ferrite/austenite interfaces retards austenite grain growth. Al alloying also suppresses diffusion of carbon and further retards the dissolution of carbides as well as austenite transformation. Consequently, the entire microstructure evolution upon superplastic forming is slowed down by Al alloying and a fine-grained microstructure is maintained during the high temperature tensile tests. Due to the fine grain size, void growth is also reduced and premature failure is prevented, promoting larger superplastic elongations. As a result of these synergistic influences of Al on the microstructure evolution, a superplastic elongation of 720% has been realized at 1053 K ($Ae_1 \sim 1033$ K).

References

[1] Jong MD, Rathenau GW. Acta Metall 1959;7:246.
[2] Takei H, Nakasa K. J Jpn Inst Met 1971;35:1063.
[3] Oyama T, Sherby OD, Wadsworth J, Walser B. Scr Metall 1984;18:799.
[4] Sherby OD, Oyama T, Kum DW, Walser B, Wadsworth J. J Met 1985;37:50.
[5] Tsuzaki K, Sato E, Furimoto S, Furuhara T, Maki T. Scr Mater 1999;40:675.
[6] Shin DH, Park KT, Kim YS. Scr Mater 2003;48:469.
[7] Valiev RZ, Langdon TG. Prog Mater Sci 2006;51:881.
[8] Zhilyaev AP, Langdon TG. Prog Mater Sci 2008;53:893.
[9] Tsuji N, Ueji R, Minamino Y, Saito Y. Scr Mater 2002;46:305.
[10] Ohmori A, Torizuka S, Nagai K. ISIJ Int 2004;44:1063.
[11] Okitsu Y, Takatab N, Tsuji N. Scr Mater 2009;60:76.
[12] Zhang H, Zhang L, Cheng X, Bai B. Acta Mater 2010;58:6173.
[13] Zhang H, Zhang L, Cheng X, Xu L, Bai B. Scr Mater 2010;62:798.
[14] Wadsworth J, Sherby OD. J Mater Sci 1978;13:2645.
[15] Sherby OD. ISIJ Int 1999;39:637.
[16] Zhang H, Bai B, Raabe D. Acta Mater 2011;59:5787.
[17] Leseur DR, Syn CK, Whittenberger JD, Sherby OD. Metall Mater Trans A 1999;30:1559.
[18] Jang YS, Phaniraj MP, Kim DI, Shim JH, Huh MY. Metall Mater Trans A 2010;41:2078.
[19] Taleff EM, Nagao M, Higashi K, Sherby OD. Scr Mater 1996;34:1919.
[20] Radis R, Kozeschnik E. Model Simul Mater Sci Eng 2010;18:1.
[21] Palizdar Y, Cochrane RC, Brydson R, Bygrave F, Scott AJ. J Phys Conf Ser 2008;126:012019.
[22] Thermo-Calc User's Guide, Version R. Stockholm: Thermo-Calc software AB and foundation of computational thermodynamics; 1995–2006.
[23] Thermodynamic database TCFE5-TCS steels/Fe-alloys database, version 5, Thermo-Calc software. <http://www.Thermocalc.com>.
[24] Sato H, Zaefferer S. Acta Mater 2009;57:1931.
[25] Calcagnotto M, Ponge D, Raabe D. Mater Sci Eng A 2010;527:2738.
[26] Thomas I, Zaefferer S, Friedel F, Raabe D. Adv Eng Mater 2003;5:566.
[27] Humphreys FJ, Bate PS, Hurley PJ. J Microsc 2001;201:50.
[28] Zaefferer S, Wright SI, Raabe D. Metall Mater Trans A 2008;39:374.
[29] Calcagnotto M, Adachi Y, Ponge D, Raabe D. Acta Mater 2011;59:658.
[30] Marquis EA, Choi P, Danoix F, Kruska K, Lozano-Perez S, Ponge D, et al. Microsc Today 2012;20:44.
[31] Dmitrieva O, Ponge D, Inden G, Millán J, Choi P, Sietsma J, et al. Acta Mater 2011;59:364.
[32] Raabe D, Sandlöbes S, Millán J, Ponge D, Assadi H, Herbig M, et al. Acta Mater 2013;61:6132.
[33] Thompson K, Lawrence D, Larson DJ, Olson JD, Kelly TF, Gorman B. Ultramicroscopy 2007;107:131.

[34] Miller MK, Cerezo A, Hetherington MG, Smith GDW. Atom probe and field ion microscopy. New York: Oxford University Press; 1996.

[35] Miller MK. Atom probe tomography: analysis at the atomic level. New York: Kluwer Academic/Plenum; 2000.

[36] Moody MP, Stephenson LT, Ceguerra AV, Ringer SP. Microsc Res Technol 2008;71:542.

[37] Seol JB, Raabe D, Choi P, Im YR, Park CG. Acta Mater 2012;60:6183.

[38] http://rsbweb.nih.gov/ij.

[39] Porter DA, Easterling KE. Phase transformations in metals and alloys. 2nd ed. Cheltenham: Nelson Thornes; 1992.

[40] Sauvage X, Quelennec X, Malandain JJ, Pareige P. Scr Mater 2006;54:1099.

[41] Shtansky DV, Nakai K, Ohmori Y. Acta Metall 1999;47:2619.

[42] Murr L. Interfacial phenomena in metals and alloys. Reading, MA: Addison-Wesley; 1975.

[43] Kashyap BP, Mukherjee AK. Res Mech 1986;17:293.

[44] Nieh TG, Wadsworth J, Sherby OD. Superplasticity in metals and ceramics. New York: Cambridge University Press; 2005.

[45] Dieter GE. Mechanical metallurgy. SI Metric ed. London: McGraw-Hill; 1988.